Check for updates

S. Singh,* V. Kumar, V. Sharma,
D. Faccio, G. K. Samanta 2300177

Near-Video Frame Rate Quantum Sensing Using Hong–Ou–Mandel Interferometry

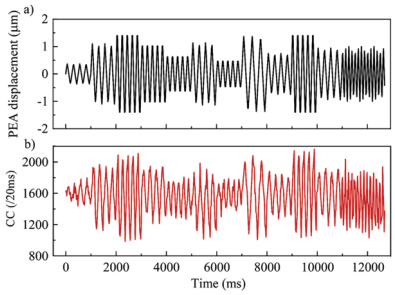

Hong–Ou–Mandel interference, has emerged as a promising tool for quantum sensing. There is a need for wide spectral-bandwidth photon pairs (for high-resolution sensing) with high brightness (for fast sensing). Here, the generation of photon-pairs with flexible spectral-bandwidth even using single-frequency, continuous-wave diode laser enabling high-precision, real-time quantum sensing is shown.

ADVANCED QUANTUM TECHNOLOGIES
www.advquantumtech.com

Near-Video Frame Rate Quantum Sensing Using Hong–Ou–Mandel Interferometry

Sandeep Singh, Vimlesh Kumar, Varun Sharma, Daniele Faccio, and G. K. Samanta*

Hong–Ou–Mandel (HOM) interference, bunching of two indistinguishable photons on a balanced beam-splitter, has emerged as a promising tool for quantum sensing. There is a need for wide spectral-bandwidth photon pairs (for high-resolution sensing) with high brightness (for fast sensing). Here, the generation of photon-pairs with flexible spectral-bandwidth even using single-frequency, continuous-wave diode laser enabling high-precision, real-time sensing is showed. Using 1-mm-long periodically-poled KTP crystal, degenerate, photon-pairs with spectral-bandwidth of 163.42±1.68 nm are produced resulting in a HOM-dip width of 4.01±0.04 μm to measure a displacement of 60 nm, and sufficiently high brightness to enable the measurement of vibrations with amplitude of 205 ± 0.75 nm and frequency of 8 Hz. Fisher-information (FI) and maximum likelihood estimation enables optical delay measurements as small as 4.97 nm with precision (Cramér–Rao bound) and accuracy of 0.89 and 0.54 nm, respectively, therefore showing HOM sensing capability for real-time, precision-augmented, in-field quantum sensing applications.

1. Introduction

Quantum sensing and metrology is a rapidly growing field due to its outstanding features in measuring physical parameters with great precision and accuracy, outperforming the pre-existing technologies based on the principles of classical physics.[1] In recent years, quantum sensing has enabled the measurement of several key physical quantities, including the measurement of the electrical field,[2] magnetic field,[3] vacuum,[4] temperature,[5] and pressure[6] with unprecedented precision and accuracy. Among various quantum sensors, as presented in ref. [7], Hong–Ou–Mandel (HOM) interferometry, since its discovery,[8] has found a large number of applications within quantum optics for a variety of advantages, including easy development and implementation, sensitivity only to photon group delay, and not phase shifts.[9]

HOM interference, purely a non-classical phenomenon, is observed for two photons that are identical in all degrees of freedom, including spin, frequency, and spatial mode, when simultaneously entering on a lossless, 50:50 beam splitter through different input ports bunch together into one of the output ports. The coincidence probability between the two output ports shows a characteristic low or zero coincidence, known as the HOM interference dip, directly related to the level of indistinguishability or the degree of purity of the photons.[10] As a result, the change in coincidence counts can be treated as a pointer to estimate the time delay between photon properties, forming the basis of the HOM interferometer-based quantum sensors to sense any physical process influencing the photon delay. As such, efforts have been made to use the HOM-based quantum sensors to characterize the single photon sources,[11] precise measurement of time delays between two paths,[8,12,13] characterization of ultrafast processes,[14] measurement of frequency shifts,[15,16] and the spatial shift.[17] On the other hand, the use of Fisher information (FI), a measure of the mutual information between the interfering photons, has enabled the maximum precision to access a lower limit decided by the Cramér–Rao bound.[18,19] In fact, the use of peak FI of the HOM interferometer, the point of maximum sensitivity, has enabled five orders of magnitude enhancement in the resolution of time delay measurements.[12,13,20] A typical FI-based measurement approach involves tuning the HOM interferometer for the peak FI point and performing iterative measurements to estimate any optical delay between the two photons. However, the number of iterations/measurements and hence the total time needed to reach the targeted precision decreases with the increase of FI value. On the other hand, the FI value can be increased by optimizing the parameters affecting the visibility and the width of the HOM interference dip. Despite the experimental demonstration of nanometer path length (few-attosecond timing) precision[12,21] and a recent theoretical study on the tailoring of the spectral properties[22,23] of photon pairs to achieve precision beyond the value reported in the laboratory condition, the width of the HOM interference dip governed by the bandwidth of the pair

S. Singh, V. Kumar, V. Sharma, G. K. Samanta
Photonic Sciences Lab.
Physical Research Laboratory
Ahmedabad, Gujarat 380009, India
E-mail: sandeep@prl.res.in
S. Singh
Indian Institute of Technology-Gandhinagar
Ahmedabad, Gujarat 382424, India
D. Faccio
School of Physics and Astronomy
University of Glasgow
Glasgow G12 8QQ, UK

The ORCID identification number(s) for the author(s) of this article can be found under https://doi.org/10.1002/qute.202300177

DOI: 10.1002/qute.202300177

 © 2023 Wiley-VCH GmbH

25119044, 0, Downloaded from https://onlinelibrary.wiley.com/doi/10.1002/qute.202300177 by <Shibboleth>-member@gla.ac.uk, Wiley Online Library on [24/09/2023]. See the Terms and Conditions (https://onlinelibrary.wiley.com/terms-and-conditions) on Wiley Online Library for rules of use; OA articles are governed by the applicable Creative Commons License

photons remained the limiting factor for optimal measurement precision[12,13,24,25] in HOM interferometer based dynamic (real-time) or fast sensing applications. As such, ultra-broadband photon sources have long been hailed as a vital prerequisite for ultra-precise HOM interferometry. While the dynamic sensing process requires the single-photon source to have high brightness. On the other hand, a new strategy has been reported very recently where the frequency entangled photons have been used to produce the HOM beating effect.[21] As the frequency of the beating is proportional to the frequency detuning of the entangled photons,[21,26] the HOM beating, in conjunction with FI analysis, enabled the measurement of low-frequency (0.5–1 Hz) vibration with a precision of ≈2.3 nm using low (18 000) number of photons pairs.[21] Despite the commendable precision measurement, such a strategy needs photons at two different wavelengths (one of them in infrared) and corresponding photon detection systems.

Nonlinear spontaneous parametric downconversion (SPDC)[27,28] process-based sources, where the annihilation of a high energy pump photon produces two daughter photons simultaneously, have evolved as a workhorse for quantum optics experiments, including HOM-based sensors. However, the development of high brightness single-photon source requires a nonlinear crystal with high figure-of-merit (FOM),[29] long crystal length, and high intensity of the pump beam. As such, periodically poled nonlinear crystals can be used due to their high intrinsic FOM. However, the increase in the crystal length reduces the spectral bandwidth of the single-photon source. On the other hand, the increase of input pump intensity and spectral bandwidth of the generated photons using ultrafast laser[30] has its own limitations in terms of expensive and bulky system architecture for any practical on-field uses. Therefore, it is imperative to explore a continuous-wave (CW) pump-based bright single-photon source with high brightness and spectral bandwidth for ultra-precise HOM interferometry.

Recently, we reported a CW pumped high brightness, degenerate single-photon source at 810 nm using periodically-poled potassium titanyl phosphate (PPKTP) crystal in non-collinear, type-0, phase-matched geometry.[31,32] Using the same phase-matching geometry, here, we report on the experimental demonstration showing the dependence of spectral bandwidth of degenerate SPDC photons and subsequent change in the HOM interference dip width on the length of the PPKTP crystal. Pumping the PPKTP crystal of length 1 mm, using a single-frequency, CW diode laser at 405.4 nm, we observed the spectral width of the SPDC photons to be as high as 163.42 ± 1.68 nm producing a HOM interference dip having a full-width-at-half-maximum (FWHM) as small as 4.01 ± 0.04 µm. Using such a small HOM interference dip width, we have dynamically measured the threshold vibration amplitude corresponding to the optical delay (twice the vibration amplitude of the piezo mirror) introduced between the photons as small as 205±0.75 nm at a frequency as high as 8 Hz. On the other hand, the reduction of crystal length from 30 to 1 mm shows a 17 times enhancement in the magnitude of the peak FI value and achieves a targeted precision (say ≈5 nm or ≈16.7 attosecond optical delay) for a number of iterations/measurements (or the total experiment time) as low as 3300 (19 min). The experimental value of the FI throughout the report, if otherwise not defined, represents the FI of a single measurement/iteration. Completion of each measurement/iteration requires 100 ms.

2. Theoretical Background

The spectral brightness of SPDC photons generated from a nonlinear crystal of length, L can be expressed as follows

$$I_{\mathrm{SPDC}} \approx \mathrm{sinc}^2(\Delta kL/2) \tag{1}$$

where Δk is the momentum mismatch among the interacting photons (pump and downconverted pair-photons) given as follows

$$\Delta k = k_{\mathrm{p}} - k_{\mathrm{s}} - k_{\mathrm{i}} - \frac{2\pi m}{\Lambda} \tag{2}$$

Here, $k_{\mathrm{p,s,i}} = \frac{2\pi n_{\mathrm{p,s,i}}}{\lambda_{\mathrm{p,s,i}}}$ is the wavevector and $n_{\mathrm{p,s,i}}$ is the refractive index of the nonlinear crystal for the pump, λ_{p}, signal, λ_{s}, and idler, λ_{i}, wavelengths. Λ is the grating period of the periodically-poled nonlinear crystal to satisfy the quasi-phase-matching (QPM) condition. The odd integer number, m, is the QPM order. For maximum efficiency, we consider $m = 1$. The momentum mismatch between degenerate photons around the central angular frequency, $\omega_{\mathrm{p}}/2$, can be represented as[33,34]

$$\Delta k = \Delta k|_{\omega=\omega_{\mathrm{p}}/2} + M|_{\omega=\omega_{\mathrm{p}}/2}\Delta\omega + \frac{1}{2}K|_{\omega=\omega_{\mathrm{p}}/2}\Delta\omega^2 + \cdots. \tag{3}$$

Assuming the QPM is achieved at degenerate SPDC photons with angular frequencies of pump, signal, and idler as ω_{p}, ω_{s}, and ω_{i}, respectively, for the grating period, Λ, the first term of the right-hand of Equation (3) can be made zero. In this situation, owing to the energy conservation, $\omega_{\mathrm{p}} = \omega_{\mathrm{s}} + \omega_{\mathrm{i}}$, the spectral bandwidth of the downconverted photons for the fixed pump frequency defined as $\Delta\omega = \Delta\omega_{\mathrm{s}} = -\Delta\omega_{\mathrm{i}} = \omega - \omega_{\mathrm{p}}/2$, is decided by the second term, $\mathrm{M} = [\partial k_{\mathrm{s}}/\partial\omega - \partial k_{\mathrm{i}}/\partial\omega]_{\omega=\omega_{\mathrm{p}/2}}$, known as group-velocity mismatch. However, for degenerate ($\omega_{\mathrm{s}} = \omega_{\mathrm{i}} = \omega_{\mathrm{p}}/2$), type-0 SPDC process, the group-velocity mismatch term vanishes or has negligible value. Under this condition, the spectral acceptance bandwidth of the SPDC photons is essentially determined by the much smaller third term of Equation (3), commonly known as group-velocity dispersion with a mathematical form $K = \partial^2 k/\partial\omega^2|_{\omega=\omega_{\mathrm{p}/2}}$. Under this condition, the spectral bandwidth of the SPDC photons can be written as

$$\Delta\omega \propto \frac{1}{\sqrt{KL}} \tag{4}$$

Thus, one can utilize the length of the nonlinear crystal as the control parameter in the SPDC process to generate paired photons of broad spectral bandwidth near the degeneracy. On the other hand, it is well known that the optical delay range or the width, σ, of the HOM interference is proportional to the coherence length of the photon wave packets[9,35] or the ensemble dephasing time of SPDC photons [36] bunching on the beam splitter. Although one can find the width, σ, of the HOM interference dip from the Fourier transform of the spectral density function of the paired photons,[37,38] we used the coherence length, L_{c}, of

© 2023 Wiley-VCH GmbH

25119044, 0, Downloaded from https://onlinelibrary.wiley.com/doi/10.1002/qute.202300177 by <Shibboleth>-member@gla.ac.uk, Wiley Online Library on [24/09/2023]. See the Terms and Conditions (https://onlinelibrary.wiley.com/terms-and-conditions) on Wiley Online Library for rules of use; OA articles are governed by the applicable Creative Commons License

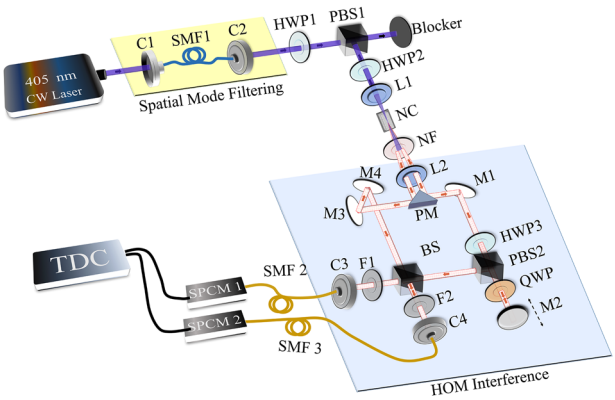

Figure 1. Schematic of the experimental setup. C1-4: fiber coupler, SMF1-3: single-mode fiber, HWP1-2: half-wave plate, PBS1-2: polarizing beam splitter cube, L1-2: lenses, NC: PPKTP crystal of grating period = 3.425 µm, NF: notch filter, PM: prism mirror, M1-4: dielectric mirrors, QWP: quarter wave plate, BS: 50:50 beam splitter cube, F1,2: high-pass filter, SPCM1-2: single photon counting module, TDC: time-to-digital converter.

the photon wave packets and Equation (4) to find the dependence of HOM interference dip width on the crystal length as

$$\sigma \approx L_c \propto 2\pi c\sqrt{KL} \tag{5}$$

where c is the speed of light in vacuum. It is evident from Equation (5) that the width, σ, of the HOM interference dip can be controlled by simply varying the crystal length even in the presence of the single-frequency, CW diode laser as the pump.

3. Experimental Setup

The schematic of the experimental configuration is shown in **Figure 1**. A single-frequency, CW diode laser providing 20 mW of output power at 405.4 nm is used as the pump laser in the experiment. The spatial mode filtering unit comprised of a pair of fiber couplers (C1 and C2) and a single-mode fiber (SMF1) is used to transform the laser output into a Gaussian (TEM_{00} mode) beam profile. The laser power in the experiment is controlled using a combination of $\lambda/2$ plate (HWP1) and a polarizing beam splitter cube (PBS1). The second $\lambda/2$ plate (HWP2) is used to adjust the direction of linear polarization of the pump laser with respect to the orientation of the crystal poling direction to ensure optimum phase matching conditions. The pump laser is focused at the center of the nonlinear crystal (NC) using the plano-convex lens, L1, of focal length, $f1 = 75$ mm to a beam waist radius of $w_o = 29$ µm. Periodically poled $KTiOPO_4$ (PPKTP) crystals of 1×2 mm^2 aperture but of five different interaction lengths, $L = 1$, 2, 10, 20, and 30 mm, are used as the nonlinear crystal (NC) in the experiment. The crystals have a single grating period of $\Lambda = 3.425$ µm corresponding to the degenerate, type-0 ($e \rightarrow e + e$) phase-matched parametric downconversion (PDC) of 405 nm at 810 nm. To ensure quasi-phase-matching, the PPKTP crystals are housed in an oven whose temperature can be varied from room temperature to 200 °C with temperature stability of ±0.1 °C.

The down-converted photon pairs, after separation from the pump photons using a notch filter (NF), are collimated using the plano-convex lens, L2 of focal length, $f2 = 100$ mm. Due to the non-collinear phase-matching, the correlated pair (commonly identified as "signal" and "idler") of downconverted photons have annular ring spatial distribution with signal and idler photons on diametrically opposite points. Using a prism mirror (PM), the signal and idler photons are separated and guided in two different paths and finally made to interact on the two separate input ports of a balanced beam splitter (BS). Since we need to vary temporal delay between the photons at the BS, and the translation of the optical component disturbs the alignment, we have devised the alignment preserving delay path consisting of a mirror, M1, $\lambda/2$ plate (HWP3), PBS2, $\lambda/4$ plate (QWP), mirror, M2 on the delay stage, and finally, the beam splitter, BS. The $\lambda/2$ plate rotates the photon's polarization state from vertical to horizontal to ensure complete transmission through PBS2. The $\lambda/4$ having the fast axis at +45° to its polarization axis transforms the photon polarization (horizontal) into circular (left circular). However, the handedness of the photon polarization gets reversed (right circular) on reflection from the mirror, M2, at normal incidence. On the return pass through the $\lambda/4$ plate, the right circular polarized photons convert into vertical polarized photons and are subsequently reflected from the PBS2 to one of the input ports of the BS. Due to the normal incident of the photons on the moving mirror, M2, the varying delay of the photons does not require tweaking of the experiment. The combination of the piezo-electric actuator (PEA) (NF15AP25), placed on a motorized linear translation stage (MTS25-Z8), is used to provide both fine and coarse optical delay. The range (resolution) of the PEA and motorized linear stage, as specified by the product catalog, is 25 µm (0.75 nm) and 25 mm (29 nm), respectively. Throughout the report, the optical delay of the photon is twice the displacement of the mirror, M2, if otherwise mentioned. On the other hand, the photons of the other arm are guided using mirrors, M3 and M4, to the second input port of BS such that the optical path length of both arms is the same. The photons from the output ports of the BS, after being extracted by long pass filters (F1, F2), are coupled into the single mode fibers, SMF2 and SMF3, through the fiber couplers, C3 and C4, respectively. The collected photons are detected using the single-photon counting modules, SPCM1-2 (AQRH-14-FC, Excelitas), and counted using the time-to-digital converter (TDC). All optical components used in the experiment are selected for optimum performance at both the pump and SPDC wavelengths. All the data is recorded at a typical pump power of 0.25 mW with a coincidence window of 1.6 ns.

4. Characterization of HOM Interference

First, we verified the dependence of HOM characteristics on the length of the nonlinear crystal. Keeping the input pump power to the crystal and the temporal coincidence window of the TDC constant at 0.25 mW and 1.6 ns, respectively, we have recorded the variation of coincidence counts as a function of the relative optical delay between the photons. As evident from **Figure 2**a, the variation of coincidence counts with the relative optical path delay has the characteristic HOM interference dip profile, approximated by an inverted Gaussian function (owing to the temporal Gaussian profile of signal and idler). However, it is interesting to note that the HOM visibilities, calculated using the formula given in ref.

© 2023 Wiley-VCH GmbH

25119044, 0, Downloaded from https://onlinelibrary.wiley.com/doi/10.1002/qute.202300177 by <Shibboleth>-member@gla.ac.uk, Wiley Online Library on [24/09/2023]. See the Terms and Conditions (https://onlinelibrary.wiley.com/terms-and-conditions) on Wiley Online Library for rules of use; OA articles are governed by the applicable Creative Commons License

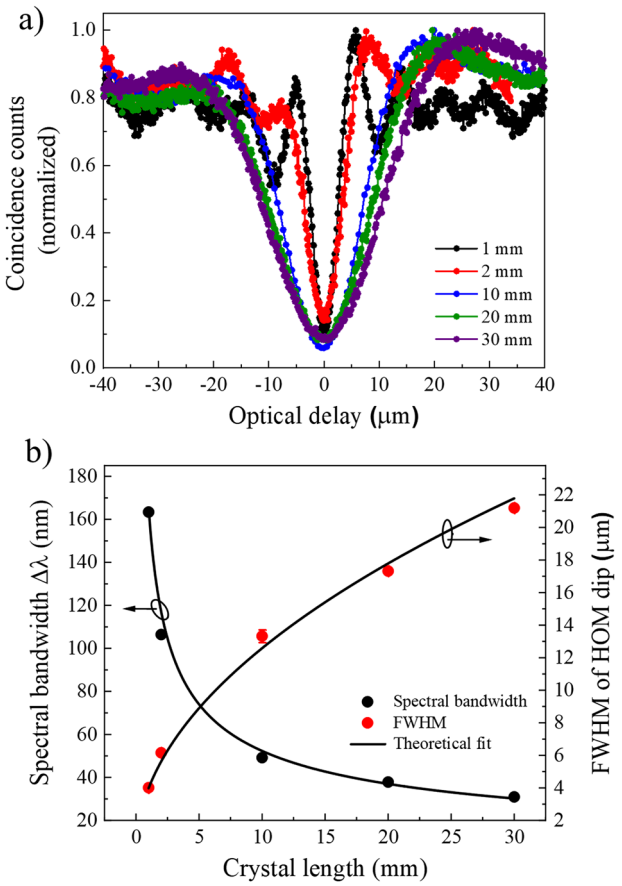

Figure 2. a) Variation of HOM interference dip profiles with the length of the non-linear crystals. b) Dependence of spectral bandwidth (black dots) and the FWHM width of HOM interference profile (red dots) of SPDC photons on the length of the non-linear crystal. The solid black line is the theoretical fit to the experimental data.

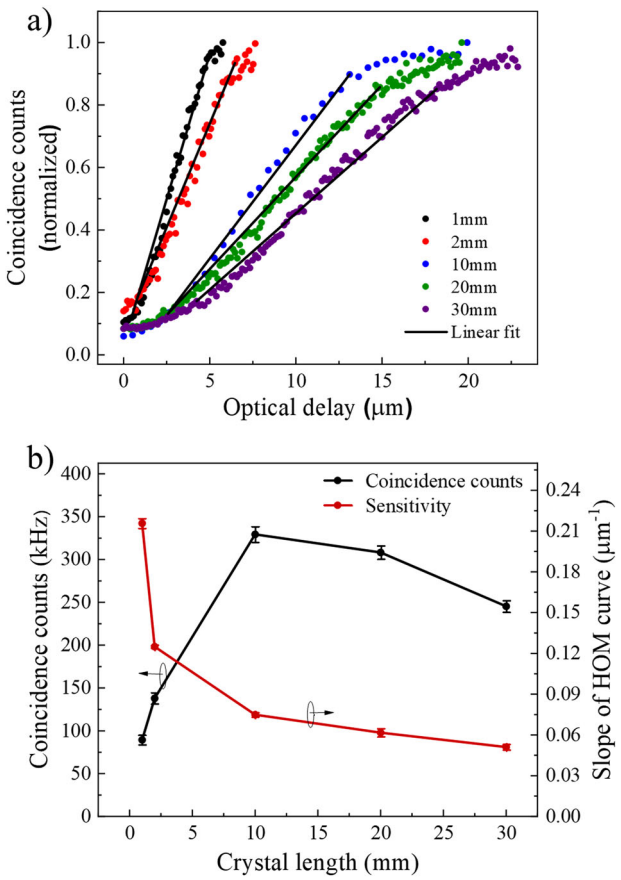

Figure 3. a) Crystal length dependent variation in the slope of coincidence counts of HOM interferometer. Solid lines are linear fit to the experimental results (dots). b) Variation of coincidence counts and slope of HOM interferometer as a function of crystal length for a fixed pump and collection beam waist radii and pump power.

[12], remain constant in the range of 86–94% despite appreciable variation in the span of the HOM interference dip profile.

To gain further insights, we measured the FWHM width of the HOM interference dip and estimated the corresponding spectral bandwidth of the photon pairs using Equations (4) and (5). The results are shown in Figure 2b. It is evident from Figure 2b that the HOM interference dip has FWHM width (red dots) of 4.01 ± 0.04, 6.16 ± 0.05, 13.33 ± 0.40, 17.32 ± 0.08, and 21.19 ± 0.13 μm corresponding to the estimated FWHM spectral bandwidth (black dots) of SPDC photons of 163 ± 1.68, 106 ± 0.93, 49 ± 1.44, 38 ± 0.20, and 30 ± 0.18 nm for the crystal lengths of 1, 2, 5, 10, 20, and 30 mm are in close agreement with the Equation (5) (solid black lines). Using the available pump power, we experimentally measured the spectral bandwidth of the SPDC photons using the spectrometer (HR-4000, Ocean Optics) to be ≈30 nm, same as our previous report[31] and ≈37 nm for 30 and 20 mm long crystals, respectively. The relatively low parametric gain has restricted the experimental measurement of the SPDC spectrum for smaller crystal lengths. However, it is important to note that the experimentally measured spectral bandwidth is matching with the estimated spectral bandwidth, as shown in Figure 2b. Interestingly, the decrease of crystal length from 30 to 1 mm results in a decrease (increase) of HOM interference dip width (spectral width of SPDC photons) by more than five times. As a result, one can see the sharp variation (see black and red dots of Figure 2a) in the coincidence counts for the small changes in the optical delay away from the zero-point optical delay for HOM interference with smaller dip width. Such amplification in the rate of change of coincidence counts with optical delay, that is, the increase of sensitivity of the HOM interferometer with the decrease in crystal length can be useful for designing HOM interferometer-based sensor to measure any physical process influencing the optical delay between the photons.

To gain further perspective, we have selected half of the HOM curve of Figure 2a, showing coincidence counts variation from minimum to maximum with positive optical delay for crystal lengths, $L = 1$, 2, 10, 20, and 30 mm. The results are shown in **Figure 3**a. Since the maximum coincidence counts per second at a fixed pump power of the HOM curve directly depend on the pair generation rate and hence the interaction length of the non-linear crystal used, for comparative study of the slopes of HOM curves for different crystal lengths, we have normalized the coincidence counts with their maxima. It is visually evident from Figure 3a that the slope of the HOM curve is gradually increasing

© 2023 Wiley-VCH GmbH

25119044, 0, Downloaded from https://onlinelibrary.wiley.com/doi/10.1002/qute.202300177 by <Shibboleth>-member@gla.ac.uk, Wiley Online Library on [24/09/2023]. See the Terms and Conditions (https://onlinelibrary.wiley.com/terms-and-conditions) on Wiley Online Library for rules of use; OA articles are governed by the applicable Creative Commons License

with the decrease of crystal length from $L = 30$ to 1 mm. However, for quantitative estimation, we have used a linear fit (solid lines) to the experimental data (points), as shown in Figure 3a, and measured the variation of the HOM dip gradient with crystal length. The results are shown in Figure 3b. It is evident that the gradient of the HOM curve decreases (red dot and line) with the crystal length from a maximum of 0.215 μm^{-1} for $L = 1$ mm to 0.051 μm^{-1} for $L = 30$ mm. Since the slope of the HOM curve reflects the measurement sensitivity, we can conclude that for the measurement of any physical parameter influencing the relative optical delay between the photons with high sensitivity, one needs a HOM interferometer with a shorter nonlinear crystal length.

However, it is well known from the literature[28,39] that the gain of the parametric process is a function of crystal length. Therefore, a decrease in crystal length to access the higher sensitivity of the HOM-interferometer-based sensor results in a decrease in the generation rate of paired photons. To get a better perspective on the generation rate of paired photons useful for quantum sensing, we have measured the coincidence counts with the change in crystal length while keeping the pump focusing waist radius ($w_p = 29$ μm) and waist radius ($w_{i/s} = 39$ μm) of the collected signal/idler constant. As shown in Figure 3b, the coincidence counts (black dot and line) for the fixed pump power of 0.25 mW increase from 89.5 to 245.3 kHz for crystal lengths ranging from $L = 1$ to 30 mm with a maximum of 329 kHz for crystal length of $L = 10$ mm. This is due to the fact that the pump focusing and collection beam waist are optimized for the crystal length, $L = 10$ mm. While one can access more counts for each crystal length by utilizing the optimum focusing conditions, it is evident from the current study that despite the use of thin crystal lengths (required for the high sensitivity of the quantum sensor), the coincidence counts are sufficiently large for practical applications. In terms of the coincidence counts, the slopes of the HOM curve for 1 and 30 mm crystals are found to be 450 and 260 μm^{-1}, respectively, at a pump power of 0.25 mW and exposure time at 20 ms. Although in the present study, we have collected the photons with a single-mode fiber, thus eliminating the photons generated in higher-order modes, it is observed in the literature[40] that the use of thin crystals can lead to the generation of broadband spatial modes. Therefore, the use of broadband spatial modes generated in the current experiment can lead to additional experiments in the future. On the other hand, here, we have used a CW diode laser to implement the system in outdoor applications. However, using an ultrafast pump laser in combination with the thin crystal for lab-based experiments, one can further enhance the sensitivity of the HOM interferometer due to the increase of overall spectral bandwidth (decrease of HOM interference dip width) of the downconverted photons and pair photon generation rate for small crystal length. Similarly, with the use of periodically-poled crystals with chirped grating, one can use long crystal lengths to generate broadband pair photons with a high generation rate.[41]

4.1. Displacement Sensing Using HOM Interferometer

Knowing the dependence of the sensitivity on the crystal length, we have studied the performance of the HOM interferometer to measure the static displacement of the mirror, introducing an optical delay between the photons. Using the 1 mm long PPKTP crystal resulting in HOM interference dip width of 4.01 ± 0.04 μm, we have moved the mirror using the motorized stage to a displacement of ≈1.25 μm away from the zero-optical delay position. This translation resulted in a positive optical delay of ≈2.5 μm corresponding to the region having maximum sensitivity of the HOM region of the sensor. We moved the mirror in a step of 60 nm (resulting in an optical delay of 200 attoseconds) and measured the coincidence counts. The results are shown in **Figure 4**. It is evident from Figure 4a, the displacement of the mirror by 60 nm results in the change of the coincidence counts of more than 50 per 20 ms of integration time. Such a large change in the coincidence count, much higher than the dark count and accidental counts, confirms the possibility of measurement of static displacement as low as 60 nm. Such a change in the coincidence count is easily detectable, confirming the displacement measurement as small as 60 nm. Further, to confirm the reliability of the measurement, we measured the temporal variation of the coincidence counts over 10 min for each mirror position. It is evident from Figure 4b that the temporal variation (with standard deviation ≈7.4%) of the coincidence counts due to various parameters, including the laser intensity fluctuation, air current, and local temperature instability in the laboratory, is much smaller than the change in the coincidence counts due to the static displacement of the mirror. The possibility of smaller static displacement can be possible by suitably reducing the fluctuation of the coincidence counts in the experiment.

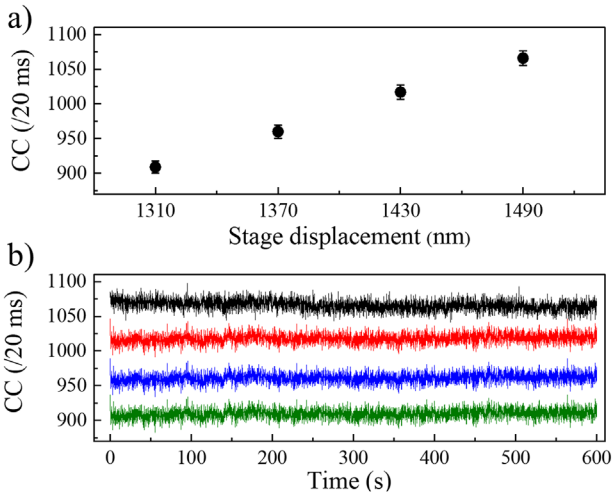

Figure 4. a) Variation in the coincidence counts (CC) with nanometer displacement of the optical delay mirror, M2. b) Temporal stability of coincidence counts at different positions of the delay-mirror, M2.

4.2. Calibration of Piezo Actuator

After successful characterization and static displacement measurement, we used a piezo-electric actuator (PEA) (NF15AP25), having a travel range of 25 μm for the applied voltage 0–75 V to study the performance of the HOM interferometer for dynamic optical delay or mirror vibration sensing applications. However, due to the unavailability of closed-loop feedback for the PEA, we had to calibrate the PEA to estimate the displacement with the applied voltage. In doing so, we have attached the mirror M2

© 2023 Wiley-VCH GmbH

25119044, 0, Downloaded from https://onlinelibrary.wiley.com/doi/10.1002/qute.202300177 by <Shibboleth>-member@gla.ac.uk, Wiley Online Library on [24/09/2023]. See the Terms and Conditions (https://onlinelibrary.wiley.com/terms-and-conditions) on Wiley Online Library for rules of use; OA articles are governed by the applicable Creative Commons License

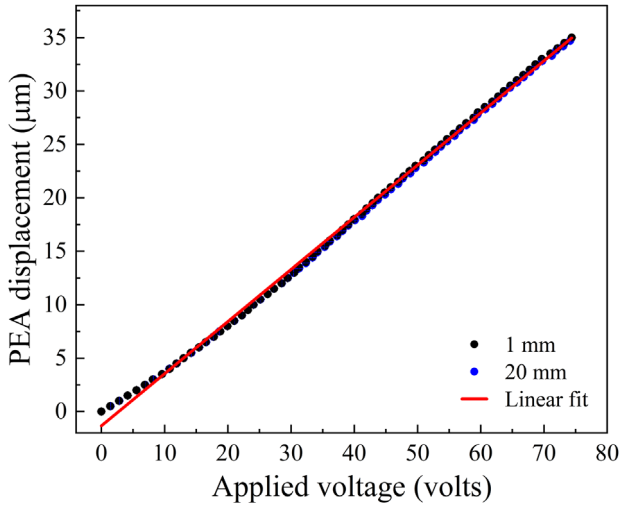

Figure 5. Linear displacement of the PEA stage as a function of applied voltage.

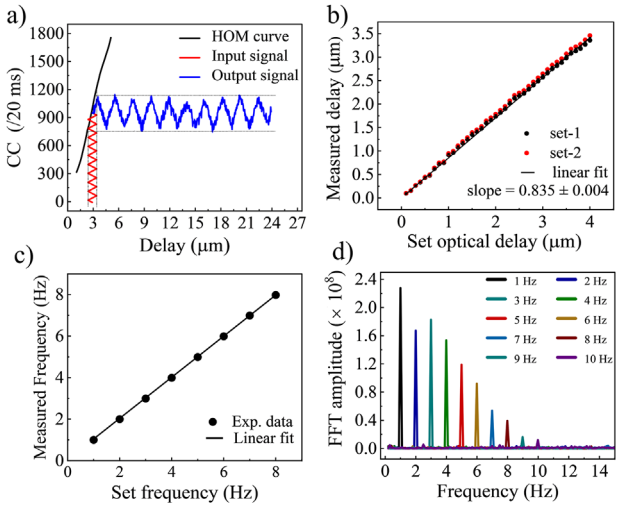

Figure 6. Vibration measurement using HOM interferometer sensor. a) Variation of coincidence counts for periodic triangular voltage signal of peak-to-peak amplitude 1 V at 1 Hz applied to the PZT stage. b) Variation of PEA displacement, and c) driving frequency measured from the coincidence counts with respect to the set values. d) Fast Fourier transformation of the time-varying coincidence counts measuring the driving frequency of the applied voltage signal.

(see Figure 1) to PEA placed over the motorized linear translation stage (MTS25-Z8). Using a crystal of length 20 mm corresponding to the HOM curve represented by the green dots in Figure 2, we have adjusted the initial position of the linear stage corresponding to a positive delay of ≈10 μm so that the coincidence count is 50% of maximum value. We moved the linear stage by ≈0.5 μm corresponding to the optical delay of ≈1 μm toward the zero-delay point, resulting in a change in the coincidence counts. Such change in the coincidence counts is reset by increasing the applied voltage to the PEA. Under this condition, the applied voltage to the PEA makes a displacement corresponding to the displacement of the linear stage in the opposite direction. We have repeated this exercise in steps of ≈0.5 μm up to the allowed PEA voltage of 75 V with the results shown in **Figure 5**. It is evident from Figure 5 that the displacement (blue dots) of the PEA is linear to the applied voltage producing a maximum displacement of 35 μm, more than the manufacturer's specification (25 μm) for the maximum allowed voltage of 75 V. Using the linear fit (red line) to the experimental data (black dots) we find the displacement of the PEA to be 0.48 ± 0.02 μm per volt. As expected, the calibration of PEA using the HOM interferometer based on a 1 mm long crystal (black dots) coincides with the results obtained using the 20 mm long crystal (blue dots).

4.3. Dynamic Vibration Sensing Using HOM Interferometer

Having the calibration data for the piezo for static displacement, we have studied the performance of the HOM interferometer for a dynamic signal. In doing so, we have used the 1 mm long PP-KTP crystal corresponding to the HOM interference dip width (FWHM) of 4.01 μm and adjusted the initial positive delay by a value of ≈3 μm. Driving the PEA with a periodic voltage signal in a triangular wavefront of controllable frequency and amplitude, we have recorded the temporal variation of the coincidence counts of the HOM with the results shown in **Figure 6**. As evident from Figure 6a, the vibrations of the PEA with a periodic triangular signal of period 1 Hz and the peak-to-peak voltage of 1 V corresponding to a peak-to-peak optical delay of ≈1.0 μm, as estimated from the calibration data of Section 4.2), produces a peak-to-peak variation in the coincidence counts of ~400 over the mean value of 960 at a period of 1 Hz, the same as the driving frequency. Further, we changed the peak-to-peak vibration amplitude of PEA from the calibration data of Figure 4.2 and measured the peak-to-peak optical delay from the coincidence counts with the results shown in Figure 6b. We have repeated this exercise twice and termed the results as set-1 (red data points) and set-2 (blue data points). As evident from Figure 6b, the peak-to-peak optical delay (which is twice the displacement of the PEA) measured using the change in the coincidence counts of HOM exactly follows the set delay at a slope of 0.835 ± 0.004. Ideally, the slope should have a value of 1 to maintain one-to-one correspondence of the set and measured values. The discrepancy between the experimental slope with respect to the ideal value can be attributed to the error in the coupling of the applied voltage to the PEA and piezo hysteresis,[42,43] which can be minimized by the unidirectional motion of the PEA and allowing sufficient relaxation time to achieve the intended position decided by the input voltage (see the PEA calibration, as shown in Figure 5, having the slope near 1). Since the slope of Figure 6b is a very important parameter for dynamic sensing applications, we have taken care of the deviation of the slope value from the ideal value in all experimental measurements throughout the manuscript. While increasing the PEA vibration amplitude through the applied voltage signal, we realized that the threshold (to replicate the shape of the input waveform exactly) peak-to-peak vibration amplitude, which can be measured dynamically using this technique, is found to be 205 ± 0.75. Subsequently, the average maximum attainable resolution between two consecutive vibration amplitudes is found to be ≈80 nm. However, one can access smaller peak-to-peak vibration amplitude (<50 nm) (without replicating the shape of the

© 2023 Wiley-VCH GmbH

25119044, 0, Downloaded from https://onlinelibrary.wiley.com/doi/10.1002/qute.202300177 by <Shibboleth>-member@gla.ac.uk, Wiley Online Library on [24/09/2023]. See the Terms and Conditions (https://onlinelibrary.wiley.com/terms-and-conditions) on Wiley Online Library for rules of use; OA articles are governed by the applicable Creative Commons License

input wavefront) from the peak-to-peak variation of the coincidence counts.

As the HOM interferometer deals with single photons, it is essential to integrate the detected coincidence events for a substantial time to get a tangible number of coincidence counts while making any measurement. Again, the required integration time is highly influenced by the brightness of the single-photon source. In the current experiment, we used high brightness single photon source based on PPKTP crystal.[31,32] As a result, we can keep the integration time as low as a few tens of milliseconds. Here, we have also tested the HOM interferometer to measure the vibration frequency of the PEA. Keeping the experimental parameters the same as previous, we have changed the frequency of the triangular voltage signal to the PEA at the constant peak-to-peak voltage of 1 V corresponding to the optical delay of ≈1.00 µm. While we adjusted the set frequency from the function generator, we recorded the temporal variation of the coincidence counts for each driving frequency and performed the fast Fourier transform (FFT) to measure the driving frequency experimentally. As evident from Figure 6c, the measured frequency using the coincidence data matches the driving frequency. The linear fit (line) to the experimental data (dots) shows a slope of 1, confirming the reliable measurement of the frequency of the driving field. However, we have restricted our measurement to 8 Hz as the FFT signal amplitude, despite having the peak at the driving frequency, as shown in Figure 6d, decreases with the increase of the driving frequency. Such a decrease can be understood as follows. In FFT analysis, the accuracy depends on the number of acquired samples from the experimental data. For example, the higher resolution in estimating the driving frequency using FFT analysis requires many data points. Again, increasing the sampling rate can increase the number of samples/data points. However, in the present case, the sampling rate is restricted to 50 Hz due to the requirement of a high exposure/integration time of 20 ms limited by the generation rate of the SPDC source and the processing speed of the TDC. Although we have 50 data points to perform FFT analysis for a driving frequency of 1 Hz, the available data points vary inverse to the driving frequency as $M = 50/f$, where M is the number of samples available for FFT analysis, and f is the driving frequency. As a result, it becomes difficult to retrace the waveform of the input signal at an increased frequency, which leads to the gradual decrease in the FFT signal amplitude (increase in signal-to-noise, SNR, value) and the subsequent appearance of its second harmonic peak. Further, an increase in the driving frequency requires a decrease in data integration time (to achieve a higher sampling rate) through the increase of the photon generation rate of the source and the use of TDC with low data acquisition latency. However, in the best-case scenario, one can, in practice, use an HOM interferometer-based sensor to measure dynamic vibration signals of unknown frequency restricted to a few tens of hertz only.

After complete characterization of the HOM interferometer-based quantum sensor in terms of static and dynamic displacement measurement, we verify its performance to measure any arbitrary vibration signal. We adjusted the initial position of the optical delay mirror, M2, like the previous studies, to access the high-sensitivity region of the HOM interference dip based on a 1 mm-long PPKTP crystal. Considering the initial position as the zero displacement point, we drove the PEA with an external voltage signal to the PEA in the triangular waveform of varying amplitude (peak-to-peak voltage range of 0.7 to 2 V) and frequency (1 to 8 Hz). The results are shown in **Figure 7**. As evident from Figure 7a, the displacement of the PEA measured from the calibration curve (see Figure 5) shows a temporal variation in both amplitude and frequency, confirming the arbitrary vibration. However, as evident from Figure 7b, the variation of the coincidence counts recorded for an integration time of 20 ms exactly follows the applied signal. Such observation confirms the possibility of measurement of any arbitrary vibration, for example, low amplitude and frequency seismic S- and P-waves, using a HOM interferometer-based quantum sensor.

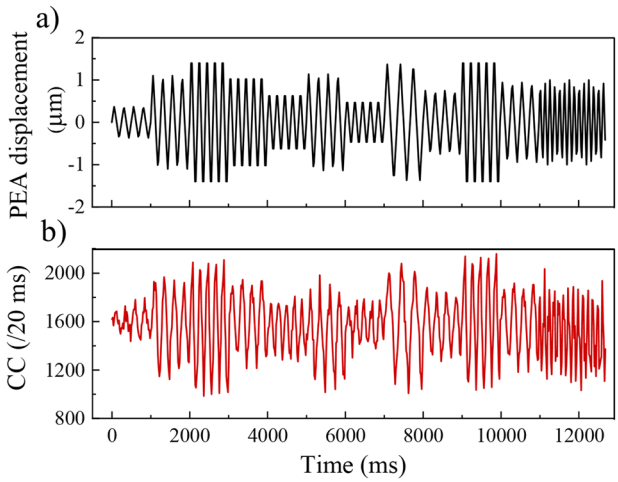

Figure 7. a) Temporal variation of PEA displacement and b) corresponding variation in the coincidence counts of the HOM interferometer for the external vibration.

The current study establishes the potential of the HOM interferometer as a quantum sensor for real-time detection of time-varying signals in the frequency ranging from 1 to 8 Hz and any physical process producing optical delays as low as 0.41 ± 0.06 µm with a precision of ≈0.19 µm. While the frequency range can further be increased to tens of hertz by reducing the exposure time of the measurement, the precision in the real-time measurement of lower optical delay is fundamentally limited by statistical and systematic error, especially at lower variation in coincidence counts.[44] As such, one needs to explore the statistical concept of Fisher information to attain a precision that has a lower limit governed by the Cramér–Rao bound.[12,13,20]

5. Precision Augmented Sensing

The ultimate limit on the precision in measurement is decided by the Cramér–Rao bound[18,19] defined as,

$$\mathrm{Var}(\tilde{x}) \geq \frac{1}{NF(x)} \tag{6}$$

where $\tilde{x}$ represents an unbiased estimator to estimate the physical parameter and $\mathrm{var}(\tilde{x})$ is the variance in the measurement. $F(x)$ represents the Fisher information (FI), a metric describing the amount of information available from a probability

© 2023 Wiley-VCH GmbH

25119044, 0, Downloaded from https://onlinelibrary.wiley.com/doi/10.1002/qute.202300177 by <Shibboleth>-member@gla.ac.uk, Wiley Online Library on [24/09/2023]. See the Terms and Conditions (https://onlinelibrary.wiley.com/terms-and-conditions) on Wiley Online Library for rules of use; OA articles are governed by the applicable Creative Commons License

distribution of an unknown parameter, for estimating the information of the parameter x in a single measurement, and N is the total number of measurements performed in the experiment. In the case of HOM interference, the mathematical form of FI is primarily determined by the temporal mode profile of the signal and idler photons.[12] As the down-converted photons generated through the type-0 SPDC process have a Gaussian spectral profile, the FI can be modeled as

$$F = \frac{4s^2\alpha^2(\gamma-1)^2(1+\gamma)}{(e^{s^2}-\alpha)(\alpha-\alpha\gamma+e^{s^2}(1+3\gamma))\sigma^2} \tag{7}$$

here, α, γ, and σ represent the HOM interference visibility, the rate of loss in photon detection, and the FWHM width of the HOM curve, respectively. $s = \frac{x}{\sigma}$ is the parameter controlling the distinguishability of the photon arriving at the beam splitter.

As evident from Equation (7), keeping all parameters constant, one can increase the magnitude of FI, F by employing the HOM interference of smaller dip width (σ). Again, it is evident from Equation (5) that for a given laser parameter, the dip width of the HOM interference varies with the square root of the crystal length. Since the crystal length, a physical parameter controllable in the experiment, using Equation (5) in Equation (7), we can derive a general expression for FI in terms of crystal length, L, as

$$F = \frac{4x^2\alpha^2(\gamma-1)^2(1+\gamma)}{A^4(e^{\frac{x^2}{A^2L}}-\alpha)(\alpha-\alpha\gamma+e^{\frac{x^2}{A^2L}}(1+3\gamma))L^2} \tag{8}$$

Here, A is a constant determined by the crystal properties. It is evident from Equation (6) that for a fixed number of measurements/iterations, N, the precision can be enhanced, or for a fixed precision, the number of measurements/iterations, N, can be reduced with the increase of the magnitude of F while saturating the Cramér–Rao bound. Therefore, Equation (8) sets the foundation for our further study of precision augmented quantum sensing. To get a better perspective on the dependence of FI on the crystal length, we have plotted Equation (8) as the function of optical delay, x, while keeping the experimentally measured values of α and γ as constant. We have used crystal lengths, L = 1, 2, 10, 20, and 30 mm, as available in our lab. The results are shown in **Figure 8**a. As evident from Figure 8a, the FI has the double-peak profiles for HOM visibility $\alpha < 1$. It has been previously observed[12] that the HOM visibility, α, influences the magnitude and the separation between two peaks of FI, respectively. However, in the current experiment, we observed that for a fixed value of HOM interference visibility, the shape and peak value of the FI depends on the value of HOM interference dip width, σ. As evident from Figure 8a, the decrease in the width of the HOM interference dip due to the decrease of crystal length (see Equation (5)) not only reduces the separation of the two peaks of FI but also shows a substantial increase in their respective peak values. To put things in perspective, using the experimental parameters in Equation (8), we estimated the peak values of FI for crystal lengths 1, 2, 10, 20, and 30 mm. The results are shown in Figure 8b. The solid dots represent the peak value of FI, calculated using experimentally measured values of α, γ, and σ for each crystal length. On the other hand, the theoretical fit to the

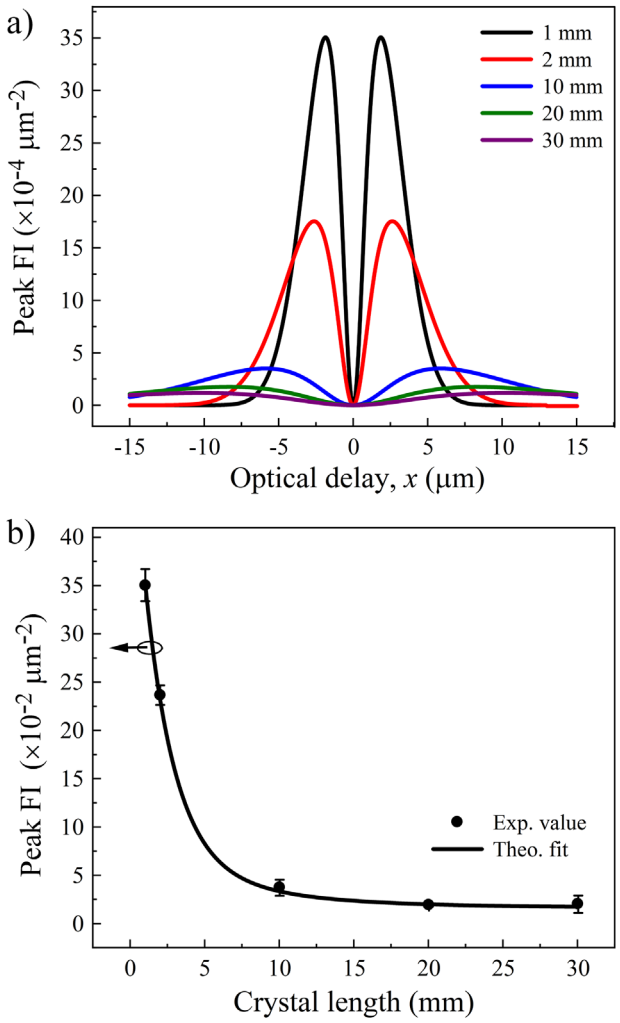

Figure 8. a) Variation of Fisher information as a function of optical delay, x, between the signal and idler photons for different crystal lengths. b) Dependence of the peak FI value with the length of the nonlinear crystal. Solid line is the theoretical fit (Equation 8) to the experimental data.

experimental results is calculated using Equation (8) for fixed values of α and γ for all crystal lengths. It is evident from Figure 8b that the peak value of FI (black dots) decreases from $35.06 \pm 1.65) \times 10^{-4}$ to $(2.07 \pm 0.19) \times 10^{-4}$ μm^{-2} for the increase of the crystal length from 1 to 30 mm due to the corresponding increase in the FWHM width of the HOM interference dip from 4.0 to 21.2 μm (see Figure 2). Such observation clearly shows the enhancement in peak value of FI (here 17×) by simply reducing the nonlinear crystal length (here 1/30) even using a single-frequency diode laser. It is also interesting to note that the current peak value of FI shows a ≈ 24× enhancement as compared to the FI value under similar measurement conditions using an ultrafast laser,[12] with the further possibility of enhancement by using an ultrafast laser generating SPDC photons in a thin nonlinear crystal. Such an increase in the peak value of FI can be useful in faster saturation of the Cramér–Rao bound as defined in Equation (6) at the lower number of measurements/iterations to achieve a predefined precision in the measurement of optical delay.

© 2023 Wiley-VCH GmbH

25119044, 0, Downloaded from https://onlinelibrary.wiley.com/doi/10.1002/qute.202300177 by <Shibboleth>-member@gla.ac.uk, Wiley Online Library on [24/09/2023]. See the Terms and Conditions (https://onlinelibrary.wiley.com/terms-and-conditions) on Wiley Online Library for rules of use; OA articles are governed by the applicable Creative Commons License

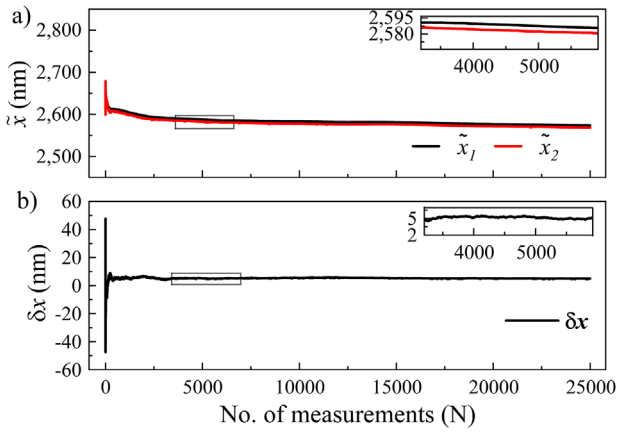

Figure 9. Variation of a) cumulative estimates for the PZT positions, x_1 and x_2, and b) the estimated optical delay between signal and idler photons as a function of the number of measurements.

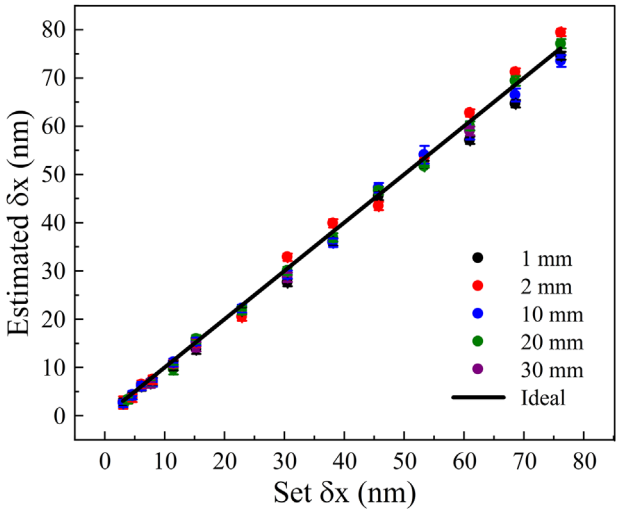

Figure 10. Variation of optical delay measured using the FI analysis with the set optical delays for different crystal lengths. Solid line represents the true values.

5.1. FI Based Measurement

The precise estimation of a physical parameter, such as optical delay, x, can be obtained through the maximum likelihood estimator.[12] In the current study, the estimator of the maximum likelihood function for measuring the optical delay can be defined as

$$\tilde{x} = \pm\sigma\sqrt{\ln\left(\frac{(N_1+N_2)}{N_1 - N_2(\frac{1+3\gamma}{1-\gamma})}\right)} \tag{9}$$

Here, N_1 and N_2 represent singles and coincidence counts, respectively. The optical delay introduced between the signal and idler photons can be estimated using Equation (9) with the proper knowledge of N_1 and N_2. To perform the FI-based measurements on the small optical delay between the paired photons, we first calibrated the 1 mm long PPKTP crystal-based HOM interferometer to estimate the parameters, α, γ, and σ. We performed 16 scans of the HOM dip to ascertain the precise values of these defining parameters of the HOM interferometer. We tried to resolve between two selected points on the HOM interference curve having the positive optical delays of, say, x_1 and x_2 with a separation of ≈5.51 nm apart. The optical delay corresponding to the maximum peak value of FI lies between points x_1 and x_2. We set the voltage to the PEA according to the calibration data shown in Figure 5 to make the back-and-forth movement between the positions x_1 and x_2 and recorded the singles count, N_1, and coincidence counts, N_2 at both points. Although the exposure time for this iterative measurement was set to 50 ms, the electronic response and delay of the Piezo controller and TDC restricted the effective data acquisition frequency to ≈6 Hz. Using all the experimental parameters in Equation (9), we have estimated the values of x_1 and x_2 with the results shown in **Figure 9**. As evident from Figure 9a, the cumulative estimates for x_1 (black line) and x_2 (red line) with the increase in the number of iterations/measurements show a drift due to the drift in the piezo position over the measurement time. However, the separation between the estimated values of x_1 and x_2, as shown by the inset image of Figure 9a, remains almost constant. We have estimated the separation between the set points as a function of the number of iterations with the results shown in Figure 9b. As evident from Figure 9b, we observe a large uncertainty in estimating the separation between the set positions for the initial measurements, which settles quickly toward the set value with the increase in the number of measurements/iterations. For the set separation value of $\delta x \approx 5.51 \pm 0.75$ nm estimated from the difference in the applied voltage to the PEA, we measured the optical delay to be 4.97 ± 0.89 nm even for the experimental measurements/iterations as low as 3300 (as shown in the inset of Figure 9b). The achievable precision for the complete range of the measurements can be calculated as $\sqrt{\mathrm{Var}(\delta\tilde{x})/N}$, where N is the total number of independent measurements performed for the cumulative estimation. The minute drift in the cumulative estimated data (see Figure 9a), due to the drift in the piezo position over the large experiment time (as high as ≈139 min), can easily be mitigated by adjusting the frequency of back-and-forth movement of ≈6 Hz; a rate much faster than the rate of drift in the position of PEA. Despite such drift, it is to be noted that the PEA position remains well inside the region (≈200 nm), having maximum FI value, adding to the reliability of the acquired data. Although we have performed about 25,000 independent measurements over an experiment time of ≈139 min, one can easily notice from Figure 9b that the true value has been achieved through the saturation of Cramér–Rao bound for the experimental measurements/iterations as low as 3380 corresponding to the experiment time as low as ≈19 min. This was possible due to the increase of the peak FI value through manipulating the spectral bandwidth of the SPDC photons. Further reduction in the experiment time to reach such high sensitivity can be possible by further enhancing the FI using the ultrafast pump laser generating SPDC photons in thin crystals.

We repeated these measurements over a wide range of optical delays using PPKTP crystals of lengths 1, 2, 10, 20, and 30 mm. The estimated optical delays calculated from the cumulative estimates are shown in **Figure 10**. As evident from Figure 10,

© 2023 Wiley-VCH GmbH

25119044, 0, Downloaded from https://onlinelibrary.wiley.com/doi/10.1002/qute.202300177 by <Shibboleth>-member@gla.ac.uk, Wiley Online Library on [24/09/2023]. See the Terms and Conditions (https://onlinelibrary.wiley.com/terms-and-conditions) on Wiley Online Library for rules of use; OA articles are governed by the applicable Creative Commons License

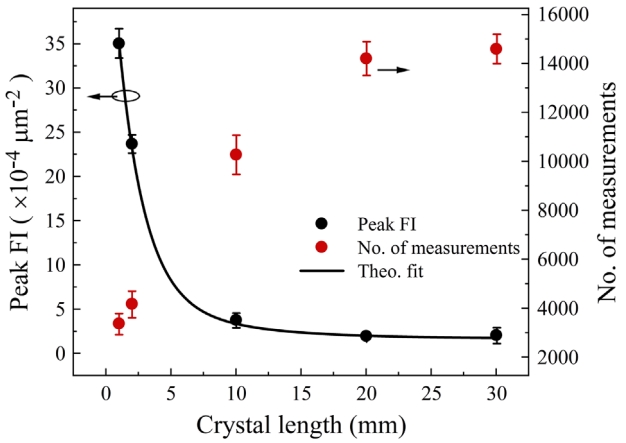

Figure 11. Variation of peak FI value and the corresponding number of iterations/measurements required to achieve a fixed precision as a function of crystal length.

the experimental values of the cumulative estimates (solid dots) of the optical delay in the range of ≈3 to ≈80 nm measured using different crystal lengths exactly follow the set true value of δx (black line) derived from the peak-to-peak amplitude of the voltage signal applied for the back-and-forth motion of the PEA. It is worth mentioning that we have incorporated the piezo hysteresis, as shown in Figure 6b, in all the measurement data. The close agreement of the experimental values of the cumulative estimate with the set true values of δx for all crystal lengths confirms the reliability and robustness of the current experimental scheme.

We further experimentally verify the dependence of the value of FI and the minimum number of required iterations/measurements while achieving a fixed precision. It is evident from Equations (6) and (8) that for a given precision, the increase in the value of peak FI reduces the required number of iterations/measurements. For experimental verification, we set, for example, the precision of the optical delay between the pair photons to be ≈5 nm and observed the minimum number of measurements/iterations (N) required to achieve this precision for all available PPKTP crystals. The results are shown in **Figure 11**. For better understanding, we have also shown the variation of the peak value of FI with crystal length. As evident from Figure 11, to achieve a set precision, the number of minimum iterations/measurements (red dots) increases from 3380 to 17500 for the increase of crystal length from 1 to 30 mm due to the subsequent decrease of peak FI value (black dots) from $\approx 35 \times 10^{-4}$ to $\approx 2 \times 10^{-4}$ μm^{-2}. It is interesting to note that the inverse of the product of the number of minimum iterations/measurements (N) and the square root of the peak value of FI forming the precision[13] is exactly matching with set precision and independent of the increase of crystal length from 1 to 30 mm. The black line is the theoretical fit to the experimental data, as reproduced from Figure 8. From this experiment, it is evident that a further increase of the peak value of FI through the increase of spectral bandwidth of the SPDC photon using an ultrafast pump can lead to the realization of FI-based ultra-sensitive measurements in real-time applications.

6. Conclusions

In conclusion, we have experimentally demonstrated easy control in the spectral bandwidth of the pair-photons through proper selection of the length of the non-linear crystal. Using a 1 mm long PPKTP crystal, we have generated paired photons with spectral width as high as 163.42±1.68 nm even in the presence of a single-frequency, CW, diode laser as the pump. The use of photon pairs with such a high spectral bandwidth in a HOM interferometer results in a narrow-width HOM interference dip enabling sensing of static displacement as low as 60 nm and threshold vibration amplitude as low as ≈205 nm with a resolution of ≈80 nm at a frequency measurement up to 8 Hz. Further, we experimentally observed the dependence of FI on the spectral bandwidth of the pair photons and, hence, the length of the nonlinear crystal. We observed a 17 times enhancement in the FI value while reducing the crystal length from 30 to 1 mm. Such an increase in the peak FI value $(35.06 \pm 1.65) \times 10^{-4}$ μm^{-2}, which is nearly 24 times higher than the previous study,[12] saturates the Cramér–Rao bound to achieve any arbitrary precision (say ≈5 nm) in a lower number of iterations (≈3300), ≈11 times lower than the previous reports. Multiplying the number of coincidence counts by the number of iterations, one can find the total number of photons used in the experiment to achieve such high precision. In our case, this provides 2×10^6 number of photon pairs to achieve the desired precision. This is somewhat higher than the 2×10^4 photons as used in the recent experiment.[21] However, our total measurement time is still lower, thanks to the high photon flux rates, therefore allowing us to achieve overall faster sampling rates and sensitivity to higher vibration frequencies. The accessibility of high precision in lower iterations or time establishes the potential of HOM-based sensors for real-time, precision-augmented, in-field quantum sensing applications. Unlike the use of bulky and expensive ultrafast pump lasers of broad spectral bandwidth to enhance the spectral bandwidth of the down-converted photons, the generation of broadband photons using a single-frequency diode laser in small crystal length is beneficial for any practical applications.

Acknowledgements

The authors acknowledge the support of Ms. Shreya Mishra, Physical Research Laboratory, Ahmedabad, for the useful discussion on statistics.

Conflict of Interest

The authors declare no conflict of interest.

Data Availability Statement

The data that support the findings of this study are available from the corresponding author upon reasonable request.

Keywords

Cramér–Rao bound, Fisher information, Hong–Ou–Mandel interference, nonlinear optics, parametric processes, quantum optics, quantum sensing

© 2023 Wiley-VCH GmbH

25119044, 0, Downloaded from https://onlinelibrary.wiley.com/doi/10.1002/qute.202300177 by <Shibboleth>-member@gla.ac.uk, Wiley Online Library on [24/09/2023]. See the Terms and Conditions (https://onlinelibrary.wiley.com/terms-and-conditions) on Wiley Online Library for rules of use; OA articles are governed by the applicable Creative Commons License

Received: June 19, 2023
Revised: August 21, 2023
Published online:

[1] S. Pirandola, B. R. Bardhan, T. Gehring, C. Weedbrook, S. Lloyd, *Nat. Photonics* **2018**, *12*, 724.
[2] K. Bian, W. Zheng, X. Zeng, X. Chen, R. Stöhr, A. Denisenko, S. Yang, J. Wrachtrup, Y. Jiang, *Nat. Commun.* **2021**, *12*, 2457.
[3] M. Tsukamoto, S. Ito, K. Ogawa, Y. Ashida, K. Sasaki, K. Kobayashi, *Sci. Rep.* **2022**, *12*, 13942.
[4] J. Hendricks, Z. Ahmed, D. Barker, P. Egan, K. Douglass, S. Eckel, J. Fedchak, N. Klimov, J. Ricker, J. Scherschligt, J. Stone, *J. Phys.: Conf. Proc.* **2018**, *1065*, 162017.
[5] K. Kakuyanagi, H. Toida, L. V. Abdurakhimov, S. Saito, *New J. Phys.* **2023**, *25*, 013036.
[6] L. Shi, Z. Li, M. Chen, Y. Qin, Y. Jiang, L. Wu, *Nat. Commun.* **2020**, *11*, 3529.
[7] C. L. Degen, F. Reinhard, P. Cappellaro, *Rev. Mod. Phys.* **2017**, *89*, 035002.
[8] C. K. Hong, Z. Y. Ou, L. Mandel, *Phys. Rev. Lett.* **1987**, *59*, 2044.
[9] A. M. Steinberg, P. G. Kwiat, R. Y. Chiao, *Phys. Rev. A* **1992**, *45*, 6659.
[10] K. N. Cassemiro, K. Laiho, C. Silberhorn, *New J. Phys.* **2010**, *12*, 113052.
[11] K. N. Cassemiro, K. Laiho, C. Silberhorn, *New J. Phys.* **2010**, *12*, 113052.
[12] A. Lyons, G. C. Knee, E. Bolduc, T. Roger, J. Leach, E. M. Gauger, D. Faccio, *Sci. Adv.* **2018**, *4*, eaap9416.
[13] Y. Chen, M. Fink, F. Steinlechner, J. P. Torres, R. Ursin, *npj Quantum Inf.* **2019**, *5*, 43.
[14] M. Lipka, M. Parniak, *Phys. Rev. Lett.* **2021**, *127*, 163601.
[15] N. Fabre, S. Felicetti, *Phys. Rev. A* **2021**, *104*, 022208.
[16] S. Restuccia, M. Toroš, G. M. Gibson, H. Ulbricht, D. Faccio, M. J. Padgett, *Phys. Rev. Lett.* **2019**, *123*, 110401.
[17] B. Ndagano, H. Defienne, D. Branford, Y. D. Shah, A. Lyons, N. Westerberg, E. M. Gauger, D. Faccio, *Nat. Photonics* **2022**, *16*, 384.
[18] C. R. Rao, *Reson. J. Sci. Educ.* **1945**, *20*, 78.
[19] H. Cramér, *Mathematical Methods of Statistics*, Vol. *26*, Princeton University Press, Princeton, NJ **1999**.
[20] N. Harnchaiwat, F. Zhu, N. Westerberg, E. Gauger, J. Leach, *Opt. Express* **2020**, *28*, 2210.
[21] S. J. Johnson, C. P. Lualdi, A. P. Conrad, N. T. Arnold, M. Vayninger, P. G. Kwiat, in *Quantum Sensing, Imaging, and Precision Metrology*, Vol. *12447*, SPIE, Bellingham, WA **2023**, pp. 263–268.
[22] K. M. Jordan, R. A. Abrahao, J. S. Lundeen, *Phys. Rev. A* **2022**, *106*, 063715.
[23] D. Triggiani, G. Psaroudis, V. Tamma, *Phys. Rev. Appl.* **2023**, *19*, 044068.
[24] H. Scott, D. Branford, N. Westerberg, J. Leach, E. M. Gauger, *Phys. Rev. A* **2020**, *102*, 033714.
[25] H. Scott, D. Branford, N. Westerberg, J. Leach, E. M. Gauger, *Phys. Rev. A* **2021**, *104*, 053704.
[26] Y. Chen, M. Fink, F. Steinlechner, J. P. Torres, R. Ursin, *npj Quantum Inf.* **2019**, *5*, 43.
[27] D. Klyshko, *ZhETF Pisma Redaktsiiu* **1967**, *6*, 490.
[28] R. W. Boyd, *Nonlinear Optics*, Academic Press, Cambridge, MA **2020**.
[29] M. Ebrahimzadeh, M. Dunn, *OSA Handbook Opt.* **2001**, *4*, 22.
[30] M. Okano, H. H. Lim, R. Okamoto, N. Nishizawa, S. Kurimura, S. Takeuchi, *Sci. Rep.* **2015**, *5*, 18042.
[31] M. V. Jabir, G. K. Samanta, *Sci. Rep.* **2017**, *7*, 12613.
[32] S. Singh, V. Kumar, A. Ghosh, A. Forbes, G. K. Samanta, *Adv. Quantum Technol.* **2022**, *6*, 2200121.
[33] R. Das, S. C. Kumar, G. K. Samanta, M. Ebrahim-Zadeh, *Opt. Lett.* **2009**, *34*, 3836.
[34] C. Chen, C. Xu, A. Riazi, E. Y. Zhu, A. V. Gladyshev, P. G. Kazansky, L. Qian, *Opt. Lett.* **2021**, *46*, 1261.
[35] A. F. Abouraddy, M. B. Nasr, B. E. Saleh, A. V. Sergienko, M. C. Teich, *Phys. Rev. A* **2002**, *65*, 053817.
[36] B. S. Ham, *arXiv:2203.13983* **2022**.
[37] P. Yepiz-Graciano, A. M. A. Martínez, D. Lopez-Mago, H. Cruz-Ramirez, A. B. U'Ren, *Photonics Res.* **2020**, *8*, 1023.
[38] M. B. Nasr, B. E. A. Saleh, A. V. Sergienko, M. C. Teich, *Phys. Rev. Lett.* **2003**, *91*, 083601.
[39] D. Ljunggren, M. Tengner, *Phys. Rev. A* **2005**, *72*, 062301.
[40] R. Ramirez-Alarcon, H. Cruz-Ramirez, A. B. U'Ren, *Laser Phys.* **2013**, *23*, 055204.
[41] M. B. Nasr, S. Carrasco, B. E. A. Saleh, A. V. Sergienko, M. C. Teich, J. P. Torres, L. Torner, D. S. Hum, M. M. Fejer, *Phys. Rev. Lett.* **2008**, *100*, 183601.
[42] M. Zhou, W. Gao, Z. Yang, Y. Tian, *J. Adv. Mech. Des., Syst., Manuf.* **2012**, *6*, 1154.
[43] D. Grzybek, A. Sioma, *Energies* **2022**, *15*, 8267.
[44] A. M. Fox, M. Fox, *Quantum Optics: An Introduction*, Vol. *15*, Oxford University Press, Oxford **2006**.

 © 2023 Wiley-VCH GmbH

25119044, 0, Downloaded from https://onlinelibrary.wiley.com/doi/10.1002/qute.202300177 by <Shibboleth>-member@gla.ac.uk, Wiley Online Library on [24/09/2023]. See the Terms and Conditions (https://onlinelibrary.wiley.com/terms-and-conditions) on Wiley Online Library for rules of use; OA articles are governed by the applicable Creative Commons License